Combined reflectance confocal microscopy-optical coherence tomography for delineation of basal cell carcinoma margins: an *ex vivo* study

Nicusor Iftimia
Gary Peterson
Ernest W. Chang
Gopi Maguluri
William Fox
Milind Rajadhyaksha

Combined reflectance confocal microscopy-optical coherence tomography for delineation of basal cell carcinoma margins: an *ex vivo* study

Nicusor Iftimia,a,* Gary Peterson,b Ernest W. Chang,a Gopi Maguluri,a William Fox,c and Milind Rajadhyakshab
aPhysical Sciences, Inc., 20 New England Business Center Drive, Andover, Massachusetts 01810, United States
bMemorial Sloan-Kettering Cancer Center, Dermatology Service, 16 East 60th Street, New York, New York 10022, United States
cCaliber I.D., 2320 Brighton Henrietta Town Line Road, Rochester, New York 14623-2708, United States

Abstract. We present a combined reflectance confocal microscopy (RCM) and optical coherence tomography (OCT) approach, integrated within a single optical layout, for diagnosis of basal cell carcinomas (BCCs) and delineation of margins. While RCM imaging detects BCC presence (diagnoses) and its lateral spreading (margins) with measured resolution of ∼1 μm, OCT imaging delineates BCC depth spreading (margins) with resolution of ∼7 μm. When delineating margins in 20 specimens of superficial and nodular BCCs, depth could be reliably determined down to ∼600 μm, and agreement with histology was within about ±50 μm. © *2016 Society of Photo-Optical Instrumentation Engineers (SPIE)* [DOI: 10.1117/1.JBO.21.1.016006]

Keywords: reflectance confocal microscopy; optical coherence tomography; basal cell carcinoma; skin cancer margins delineation.

Paper 150600R received Sep. 7, 2015; accepted for publication Dec. 14, 2015; published online Jan. 18, 2016.

1 Introduction

Basal cell carcinomas (BCCs) are among the most common malignancies in the world. Of the estimated 3.5 million new cases of nonmelanoma skin cancers that are diagnosed every year in the USA alone, about 80% are BCCs.[1,2] BCCs occur most commonly in the middle-aged and older populations, but are increasingly also affecting younger populations.[3,4] Approximately 80% to 90% of the cases occur on the head and neck. Although not fatal, BCCs can cause large-scale anatomical destruction, resulting in morbidity, physical disfigurement, loss of function, and psychological trauma.[5–7] Therefore, timely diagnosis and treatment are needed.

Mohs surgery is the standard procedure for BCC therapy in the USA, with 5-year cure rates of 98% to 99%.[8,9] Currently, an estimated 1.5 million surgeries are performed every year for nonmelanoma skin cancers (both BCCs and squamous cell carcinomas), with treatment costs of about $2 billion.[10] Mohs surgery is labor-intensive, time-consuming, and expensive. Consequently, less invasive and less expensive nonsurgical alternative therapies are being increasingly developed.[11–13] Nonsurgical therapies can be particularly effective for minimally invasive removal of superficial and nodular BCCs,[14] which constitute about 40% (600,000 per year) of the total Mohs surgical cases. With such therapies, however, there is no tissue available for immediate pathological evaluation for the presence or clearance of tumor. The lack of pathological feedback results in variable efficacy and limited cure rates.

Further advancement of such therapeutic approaches will need guidance and feedback directly on the patient: pretreatment imaging to determine the lateral and depth spreading of the cancer and to guide the choice of treatment, followed by post-treatment monitoring to determine if the tumor has been entirely removed or not and to improve the efficacy of the treatment. Therefore, various microscopic imaging and spectroscopic modalities and macroscopic approaches[15–23] are being developed to detect BCCs for diagnosis, as well as for presurgical assessment of the margins[24–35] and for providing feedback for guiding therapy. Of all these, reflectance confocal microscopy (RCM) and optical coherence tomography (OCT) appear to be particularly attractive. RCM imaging is capable of revealing nuclear, cellular, and morphologic detail in BCCs *in vivo*.[24,35,36] The main detectable diagnostic features include tumor nests in basaloid patterns with palisading and clefting, increased nuclear density, nuclear atypia in polarized patterns, and microvasculature in linear telangiectasia-like patterns, which correlate well to pathology. Clinical trials have reported that RCM can detect BCCs with sensitivity of 92% to 100% and specificity of 88% to 97%.[15,37,38] Furthermore, the feasibility of RCM for determining the lateral margins of BCCs has been reported.[38,39] Although RCM has an inherently small field of view (FOV), usually limited to about 1 × 1 mm, larger areas can be imaged and the lateral margins of the tumor can be determined by the acquisition of video mosaics.[14,15,24]

However, the penetration depth of RCM imaging is limited to 100 to 200 μm, which is not sufficient for estimating the deeper margins of BCCs. Therefore, OCT imaging, which has been proven to visualize the microanatomy of BCCs to depths of at least 1 mm,[40–45] is a complementary technology that can be used for this purpose. Superficial and nodular BCCs are particularly well-imaged with OCT. A number of observational studies have reported the ability of OCT to reliably detect the depth of BCCs.[41–45] Depth measurements with OCT are more accurate, due to its higher resolution, than those with other approaches such as ultrasound and magnetic resonance-microscopy. In addition, both OCT and RCM are optical imaging modalities, which more easily facilitates their integration into a single instrument.

*Address all correspondence to: Nicusor Iftimia, E-mail: iftimia@psicorp.com

Based on the above considerations, we hypothesized that combined RCM/OCT imaging within a single instrument can determine both the presence and also the lateral and depth margins of BCCs. While RCM imaging will diagnose and delineate the lateral margins, OCT imaging will delineate the depth margins. RCM/OCT imaging may help the dermatologist to triage the tumors into either superficial and early nodular types (when within a depth of ~500 to 600 μm, for which nonsurgical treatment would be suitable) or the deeper micronodular and infiltrative types (when deeper than ~500 to 600 μm, which would require standard Mohs surgery). Furthermore, the estimate of depth may guide the choice of treatment parameters, such as dosing in topical therapy, fluence, and number of passes for laser ablation.

We tested our hypothesis with a benchtop study, and thus we report in this paper the feasibility for combined RCM/OCT imaging to reliably detect both the lateral and depth margins of BCCs in skin samples *ex vivo* with micron-scale resolution, as well as the validation of our results by pathology reports.

2 Methods

2.1 Instrumentation

An RCM/OCT benchtop instrument was developed for the purpose of this study. The dual-modality instrument (see simplified schematic in Fig. 1) consists of four subsystems: OCT subsystem, RCM subsystem, common path RCM/OCT imaging probe, and system control and data processing unit.

The OCT subsystem is based on a polarization-sensitive scheme. The idea was to investigate both reflectance and birefringence properties of the skin and determine if birefringence images may help to more precisely determine cancer spreading relative to the dermal–epidermal junction. The instrument uses a broadband superluminescent light source (Denselight, California) with a 1310-nm central wavelength and 92-nm bandwidth. The theoretical axial resolution l_z provided by this source is about 8.2 μm in air and 6.1 μm in tissue: $l_z = 0.44\lambda_0^2/n\Delta\lambda$, where λ_0 is the center wavelength of the light source, $\Delta\lambda$ is the spectral width of the light source, and n is the refractive index of

the sample (~1.34 for biological tissues). The OCT light source includes a polarizer to provide linearly polarized light. The light from the linearly polarized light source enters a polarization maintaining (PM) fiber interferometer, where it is split by a 50/50 PM coupler (Evanescent Optics Inc., Canada) into reference and sample arms. About 30-m legs were used for the sample and reference arms to avoid the self-interference signal from the two axes of the fiber protruding into the 2.5-mm coherence range of the instrument. This value was obtained by taking into account the dispersion characteristics of the PM fibers used in our setup. In the reference arm, light exits the PM fiber via a collimator and passes a variable neutral density filter (for optimizing reference power) and a quarter wave plate (QWP) oriented at 22.5 deg, and is finally reflected by the reference mirror. After double passage of the QWP, the orientation of the polarization plane is at 45 deg to the horizontal, providing equal reference power in both channels of the polarization-sensitive detection unit. In the sample arm, after exiting the fiber through a collimator, light passes a QWP oriented at 45 deg, which provides circularly polarized light onto the sample via the imaging objective. A piece of BK7glass is used in the reference arm of the interferometer to compensate for dispersion imbalance caused by the sample arm elements, especially by the imaging objective. High-order dispersion is corrected in software using a typical scheme, which was reported by us in detail elsewhere.[46]

An X–Y galvanometer scanner is placed at the entrance pupil of a telescope that relays the scanned beam into the entrance pupil of the objective lens. After recombination of light from the reference and the sample arm at the 50/50 PM fiber coupler, light is directed to a dual channel spectrometer. This spectrometer uses a polarization beamsplitter to decouple the two orthogonal polarization states of the light to two cameras (Sensors Unlimited, Model 1024-LDH2) via a diffraction grating (1200 lines/mm).

The OCT subsystem retrieves both the reflectance and birefringence information of the sample. Birefringence information is obtained by extracting the phase retardation of the OCT signal. The phase retardation $\delta(z)$ is calculated from the total
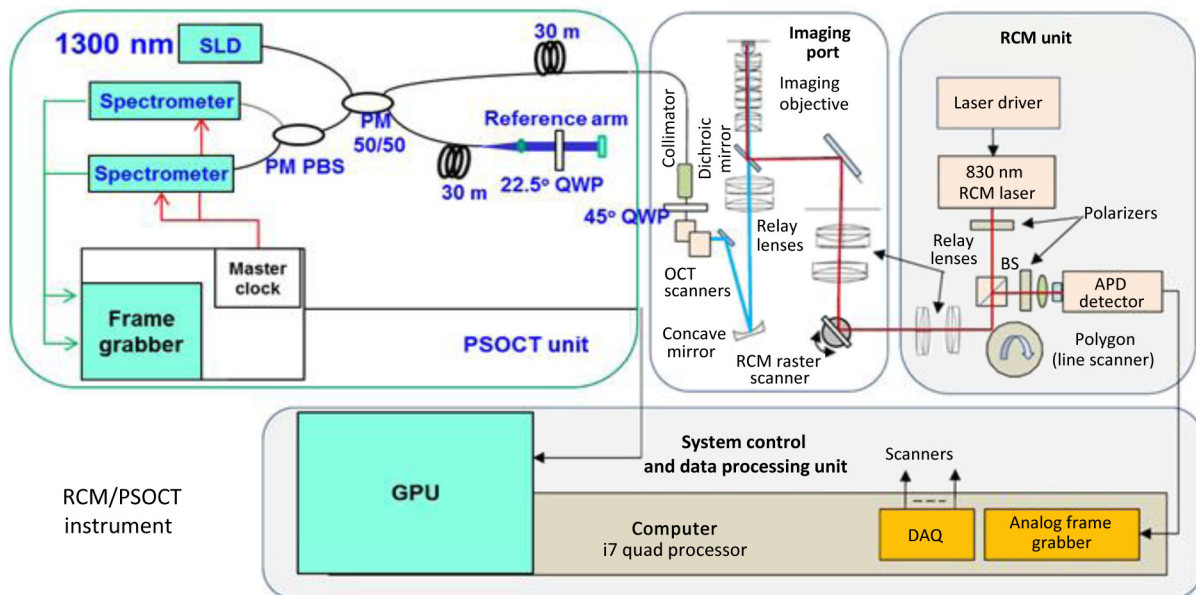

Fig. 1 Simplified schematic of the RCM/OCT instrument.

backscattered light reflectivity $R(z)$, which is encoded in the sum of the squared amplitudes of the two channels[46]

$$R(z) \sim A_1^2(z) + A_2^2(z), \quad d(z) = \arctan[A_2(z)/A_1(z)]. \quad (1)$$

The RCM subsystem uses a standard reflectance confocal scheme. The light from an 830-nm laser diode is directed by a beamsplitter cube to a set of scanners composed of a polygon scanner (Model HCAB, Lincoln Lasers) and a galvanometer scanner (Model 6200H, Cambridge Technologies, Massachusetts). The two scanners are relayed to the objective lens entrance pupil by two sets of relay lenses (telescope arrangement). The light returned from the sample is directed by the same beamsplitter cube to the avalanche photodiode (APD) detector. A pinhole is placed in front of the APD to reject the out-of-focus photons. Two polarizers are crossed in the emission and detecting paths to reduce the impact of sample specular reflections.

The common path imaging probe contains folding optics and a relay system for the OCT beam such that the OCT scanners can be relayed to the pupil plane of the objective lens. A dichroic mirror is used to combine the RCM and OCT beams into the common optical imaging path. A custom-made objective lens with a numerical aperture (NA) of 0.8 and a working distance (WD) of 1.2 mm is used. Different beam sizes are used in RCM and OCT modes to ensure optimal imaging performance. The pupil of the objective lens, 10 mm in size, is overfilled in the RCM mode, allowing for full utilization of the NA and thus for submicron lateral resolution. The theoretical lateral resolution of the RCM subsystem is about 0.53 μm ($\Delta x = 0.46\lambda/\mathrm{NA}$), while the theoretical optical sectioning is about 2.6 μm ($\Delta z = 1.4n\lambda/\mathrm{NA}^2$) for a refractive index $n = 1.33$ (water immersion). To keep the OCT imaging depth within a reasonable range (over 0.8 mm), a small OCT beam size ($D = 1.0$ mm) at the objective lens entrance pupil is used. For an effective focal length EFL of 4.5 mm (WD of 1.2 mm), the size of the OCT beam at the focus is about 7 μm ($\Delta x = 1.22\lambda F/D$). Since each OCT frame has 512 A-lines and the OCT FOV is 2 mm, about 4 μm/pixel lateral sampling resolution is achievable in OCT mode.

Both the OCT and the RCM signals are digitized and processed by a system control and data processing unit. A graphical

processing unit (GPU), model GTX 8600, that uses 1152 CUDA cores is used to expedite the OCT data processing (FFT, dispersion, and interpolation), allowing for 40 frames/sec real-time display. Thus, an OCT raster image consisting of 512 frames can be acquired in about 13 s. Since the RCM image does not need any GPU processing, the RCM imaging speed is mainly dictated by the speed of the polygon scanner. Using the Lincoln Lasers polygon scanner, Model HCAB, RCM images are collected at an imaging speed of about 10 frames/s.

Photographs of the RCM/OCT instrument are shown in Fig. 2. An inverted microscope arrangement is used to allow for ease of imaging skin specimens. A motorized X–Y stage is used to interrogate various areas of the tissue specimens and to determine the location of the BCC tumor, while a Z-stage is used to select the imaging depth or to automatically generate a stack of images at various depths.

2.2 Instrument Testing and Optimization

The RCM/OCT instrument was fully tested and optimized before performing measurements on skin cancer tissue specimens. Coregistration of the RCM and OCT images, imaging depth, sensitivity decay within the imaging range, FOV, and imaging resolution were measured and optimized.

Image coregistration was first tested using an USAF 1951 resolution target such that the center of the RCM frame corresponded to the center of the enface OCT image. For this purpose, enface OCT and RCM images were taken and the offsets were applied to the OCT beam to coalign it with the RCM beam. The lateral resolution in both modes was determined as well, using the higher-resolution USAF 6251 target. A lateral resolution of about 6 μm was measured in the OCT mode, while the RCM resolution was better than 1 μm.

The axial resolution of OCT has been evaluated by measuring the full width at the half maximum of the coherence peak. A value of 9.5 μm in air, which corresponds to $\sim$7 μm in tissue, has been measured. The difference is thought to be attributed to slight clipping of the spectrum on the spectrometer camera, thus the full bandwidth of the source was not used.

The measured FOV was 2 $\times$ 2 mm in OCT mode and 0.8 $\times$ 0.8 mm in RCM mode. The OCT FOV is mainly limited by the imaging objective. A larger FOV is desirable in OCT mode. However, this will require the use of an objective with a larger
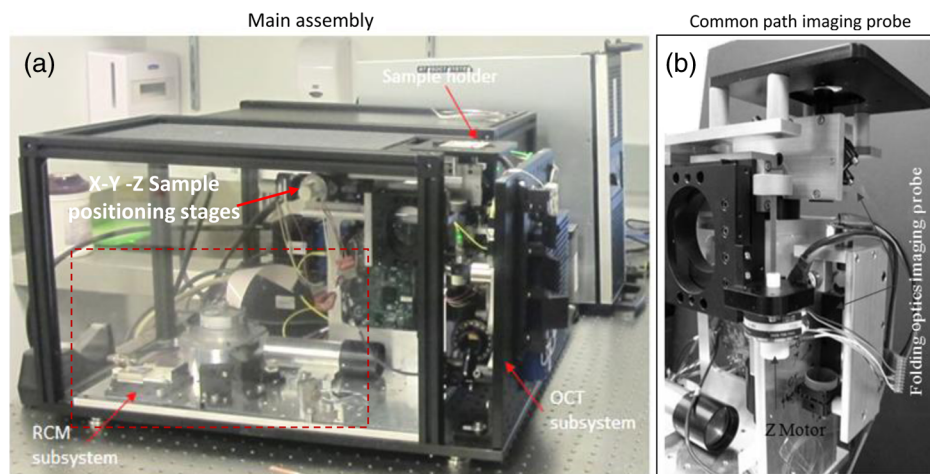

Fig. 2 Photographs of the RCM/OCT imaging instrument; (a) general view of the instrumentation unit and (b) detail of the common path RCM/OCT imaging arm.

entrance pupil and a higher WD. Unfortunately, a longer WD will also impact the NA and thus the resolution in RCM mode. A potential solution for the future is to use a second imaging objective with a lower NA, which will be used in specific cases where skin thickness and cancer spreading require a longer imaging depth.

The imaging depth and the capability of the instrument for resolving morphologic details in tissue were further tested *in vivo* in the skin of the investigators. An example of OCT/RCM images collected from a volunteer dorsal palm is shown in Fig. 3. OCT was capable of fully resolving both layers (epidermis, dermis) [see Fig. 3(b)]. The phase retardance image allowed us to determine the presence of the collagen in the dermal layer, and thus to delineate the dermal-epidermal junction in areas of the skin (dorsal palm) where it is not always easily retrievable from the reflectance image [see Fig. 3(c)]. RCM images were obtained from the red-marked area shown in Fig. 3(b) in the OCT frame. The RCM images [see Figs. 3(d) and 3(e)] demonstrate instrument capability for resolving subcellular features, such as polygonal epidermal granular and spinous cells with dark nuclei surrounded by bright cytoplasm, as well as the underlying layer of basal cells. RCM imaging depth was about 180 μm.

2.3 Tissue Specimen Procurement and Preparation

Skin tissue specimens of BCCs, obtained in the Dermatology Service at Memorial Sloan Kettering Cancer Center (MSKCC) under an Institutional Review Board–approved protocol from patients undergoing Mohs surgery, were brought to the imaging laboratory within 2 to 3 h after surgery and kept in refrigerated saline. Each specimen was placed on the RCM/OCT microscope
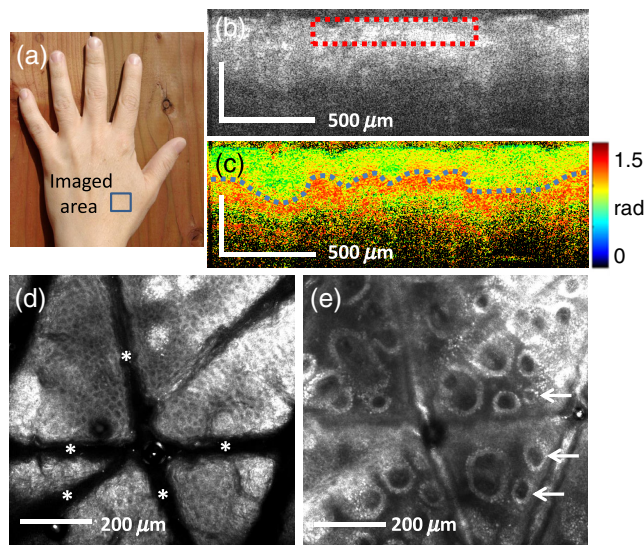
and imaging was performed while keeping the specimen hydrated. The measurement sites were marked with ink and histology was performed to correlate RCM/OCT findings with histopathology results.

3 Results

Three representative cases showing RCM/OCT capability for detecting the morphology of BCCs and delineating tumor margins are shown in Figs. 4–6.

The first case (see Fig. 4) is that of nodular BCC with an infiltrative morphological component, starting at the dermal-epidermal junction and invading the deeper dermal layers. The histology in Fig. 4(a) shows the tumor as the very dense, hyperkeratotic areas (dark purple-stained nuclei). In the OCT image, we identified the BCC clusters as very irregular darker (grey to black) areas [see Fig 4(b)]. Since the reflectance image does not show a clear differentiation between the dermal and epidermal layers, we used the phase retardance image [see Fig. 4(c)] to retrieve the location of the dermal-epidermal (DE) junction, and then, relative to this location, determined how deeply the tumor had invaded the dermal layer. On the other hand, due to tumor invasion in the dermal layer, the orientation of the collagen fibers was disrupted, and, as a result, the phase of the OCT signal exhibited lower retardation in the areas where the BCC nodules were present. Therefore, the phase retardance image alone might not provide a very good estimate of the BCC depth spreading. However, as stated above, it can complement reflectance image findings to determine the position of the DE junction. The RCM images were used to confirm that the dark areas seen in the OCT image were, in fact, BCC nodules. The difference between the normal and tumor areas of the tissue are shown in Figs. 4(d) and 4(e). Figure 4(d) of the upper epidermis shows normal polygonal epidermal cells with dark nuclei [similar to the morphology seen in Figs. 3(d) and 3(e)], while a clear BCC invasion in the underlying dermis (dark hypoechic areas) is
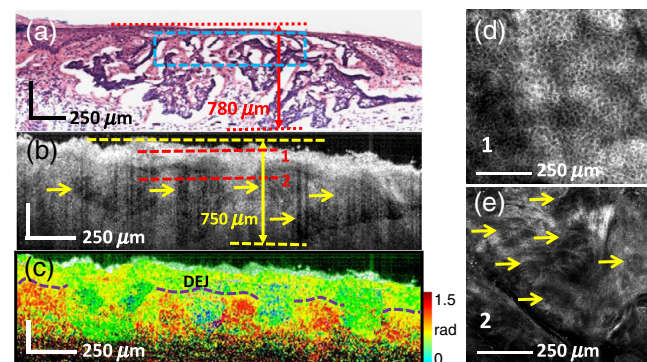

Fig. 3 Coregistered OCT/RCM images of normal skin. (a) Picture of a volunteer's dorsal palm, showing the area (blue square) where RCM/OCT imaging was performed; (b) cross-sectional OCT image. Within the red-dotted rectangle is where RCM imaging was performed; (c) OCT phase retardance image, showing the segmentation (blue-dotted line) of the dermal-epidermal junction; (d), (e) enface RCM images from the red-dotted area in A, showing granular and spinous cells in the epidermis and the underlying basal cell layer. Seen are crisscrossing dark wrinkles (asterisks in D). In between the wrinkles are the honeycomb patterns of bright cells and dark nuclei. The basal layer is seen as rings of bright basal cells [arrows point to three such rings in (e)].

Fig. 4 RCM/OCT images of nodular BCC with infiltrative components; (a) H&E-stained histology section, showing the measured depth of the tumor (780 μm) and also the area (blue-dashed rectangle) where imaging was performed; (b) cross-sectional OCT imaging showing measured depth of tumor (750 μm) and dark-appearing nodules of dermal invasion of BCC (yellow arrows). The red-dotted lines are the depth locations where enface RCM imaging was performed; (c) cross-sectional phase retardance OCT image, highlighting the dermal-epidermal junction (DEJ, blue-dashed line); (d), (e) enface RCM images of normal epidermal and basal layer (d) and multifocal BCC tumor nodules (yellow arrows) in the underlying dermis. (e) Levels 1 and 2 in the OCT image [these are located at the red-dashed lines in (b) and within the blue-dashed area in (a)] show the epidermal and dermal locations, respectively, where the RCM images (d), (e) were obtained.
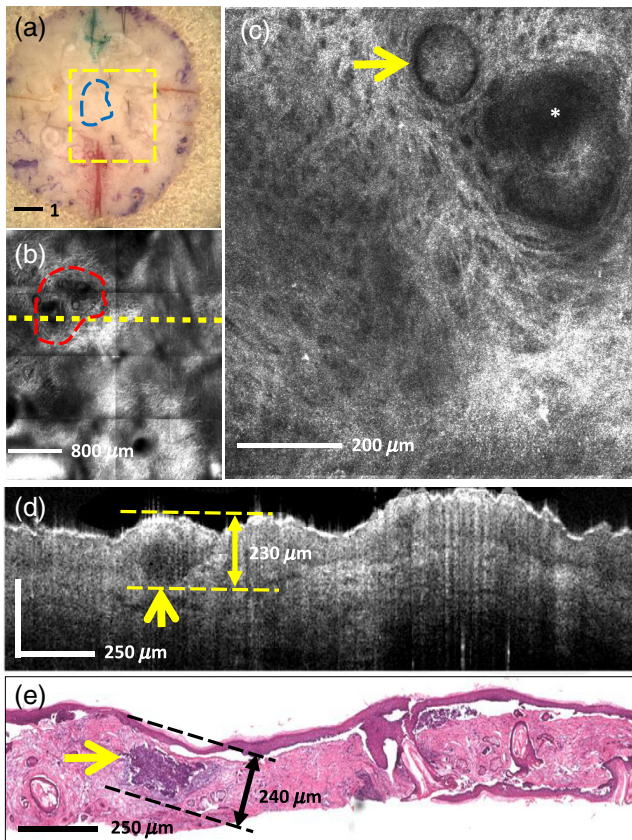
Fig. 5 Demarcation of tumor margins with RCM/OCT. (a) Clinical picture of the skin specimen, showing the area of RCM mosaicking (yellow-dotted box) and the presence of tumor (blue-dotted area); (b) enface RCM mosaic at a depth of 150 μm, showing the lateral margins of the nodular BCC tumor (red-dotted area); (c) magnified view of RCM mosaic (this is within a single RCM image), showing a tumor nodule (yellow arrow) and a sweat gland (asterisk), surrounded by collagen in the dermis. (d) Cross-sectional OCT image at the location of the yellow-dotted line in (b), showing measured depth (230 μm) and deep margin (yellow arrow) of the tumor; (e) H&E stained histology showing nodular BCCs (yellow arrow) and measured depth (240 μm).

Fig. 6 Demarcation of tumor margins with RCM/OCT. (a) Cross-sectional OCT image showing two stitched adjacent fields of view covering a 4-mm specimen. Nodular BCC tumors are seen (yellow arrows). The deep margins (yellow-dotted line) of the tumors are at approximately 550 μm. The red-dotted line is the 350 μm depth at which enface OCT mosaics (shown in b) were obtained, and the green-dotted line is the shallower approximate depth at which enface RCM mosaics [shown in (d) and (e)] were obtained; (b) enface mosaic of four OCT images at a depth of 350 μm [i.e., at the location of the red-dotted line in (a)], showing the lateral margins (yellow-dotted area) of the tumor; (c) H&E-stained histology showing nodules of BCCs (yellow arrows) to measured depth of approximately 570 μm; (d)–(e) enface RCM images from areas overlying the green-dotted squares in (b), at a relatively shallower depth [i.e., at the location of the green-dotted line in (a)], showing magnified views of the tumor. Dark-appearing nodules of tumor are seen with faintly dark-appearing nuclear morphology (green arrows).

observed in Fig. 4(e). This irregular pattern indicates the multifocal presence of the BCC.

The RCM images can also be used to precisely demarcate the lateral margins of BCCs. This is illustrated in the second case presented here [see Fig. (5)]. A clinical overview picture [see Fig 5(a)] shows the area of RCM mosaicking (yellow dashed box) and the presence of tumor (blue dashed area). A mosaic of 16 RCM images [see Fig. 5(b)] shows an area of the tissue specimen where superficial BCC nodules are present. The enface mosaic was taken at a depth of about 150 μm. The lateral margins of the nodular tumor [see red-dotted area in Fig. 5(b)] were demarcated by our clinician based on the RCM image features. A magnified view of a nodular area (yellow arrow) is shown in Fig. 5(c). The nodule is surrounded by cleft-like spaces, which do not scatter light and thus appear as a darker boundary along the outer periphery of the tumor nodule (yellow arrow). Surrounding the tumor nodule are bright fibrous bundles of collagen of dermal stroma (seen in the entire remaining area of the image). The formation of round BCC nodules is observed in the OCT image [see round hypoechic areas in the cross-sectional OCT image from Fig. 5(d)] and confirmed by the
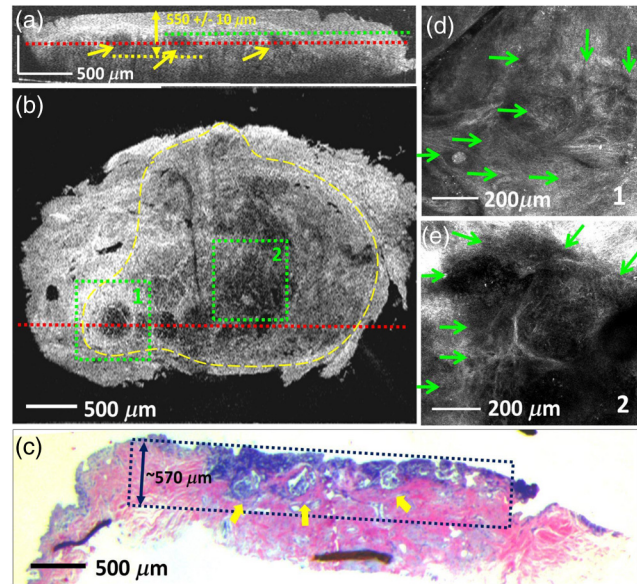
histology in Fig. 5(e). The depth (240 μm) was determined from the cross-sectional OCT image.

The third case, illustrated in Fig. 6, is that of a nodular BCC, where the formation of round tumor clusters is observed in the OCT image [see round hypoechic areas in the cross-sectional OCT image in Fig. 6(a)] and confirmed by the histology in Fig. 6(c). To demarcate both the depth and the lateral margins of the tumor over the entire specimen, we created a mosaic of four OCT images (2×2 mm each), shown in Fig. 6(b). The enface images were taken at a depth of about 350 μm, as indicated by the red-dotted line in Fig. 6(a). These images were stitched together using a texture analysis approach. The mosaic shows the formation of a cluster of BCC nodules [yellow-dotted area in Fig. 6(b)]. The RCM images [Figs. 6(d) and 6(e)] show dark nodular areas surrounded by a bright-appearing rim of stroma. This rim can be observed as well in the enface OCT mosaic [Fig. 6(b)]. In this particular case, both the depth and the lateral margins of the nodular BCC seem to be relatively well demarcated by the OCT. The depth of 550 μm indicated by OCT [Fig. 6(a)] was confirmed by histology [Fig. 6(c)].

A summary of the measurements from 20 specimens with nodular and superficial BCCs is presented in Table 1. The depth of the superficial tumor was maximum 550 μm for eight cases, which qualified as superficial or nodular BCCs, and exceeded 600 μm in 12 cases, when some tumors had an infiltrative component, as shown in Fig. 4. Since the depth of the tumor is

Table 1 Summary of RCM/OCT measurements on BCCs.

Tumor type	No. of specimens	Lateral extent (mm)	OCT-based invasion depth (μm)	Histology-based invasion depth (μm)	OCT disagreement on depth measurement (μm)
Nodular BCC	12	5 to 8	600 to 980	500 to 950	± 50
Superficial BBC	8	3 to 5	200 to 550	200 to 550	± 20

critical for our future intended application [guiding choice of treatment (nonsurgical or surgical)], we measured the depth with OCT and compared with that seen in histology.

As summarized in Table 1, small disagreement was found for the deeper nodular BCCs. One reason for OCT error is the relatively limited penetration depth provided by the current instrument, resulting in somewhat less reliable depth information when the tumor extended over 700 μm in depth. Thus a compromise has to be made between the desired RCM resolution and OCT imaging depth, such that an adequate NA imaging objective must be selected. Another, but somewhat less expected factor, may be the discrepancy between measurements in fresh tissue *ex vivo* and frozen sections. However, shrinkage of tissue is known to be minimal between excised *ex vivo* and pathology sections. Shrinkage tends to be significantly larger between *in vivo* and excised *ex vivo* conditions, since most of the shrinkage occurs when tissue is removed from a subject but not in the subsequent processing for pathology.[47]

4 Discussion and Conclusion

Our preliminary study has demonstrated the feasibility of using combined RCM/OCT within the same optical layout to determine the lateral and depth margins of superficial and nodular BCCs. RCM has proven to be effective in providing enface images with nuclear-level resolution in superficial skin to depths of about 200 μm, and thus in delineating the lateral margins of the BCCs. However, due to its limited penetration depth, it could not be used to determine deep margins. OCT has proven to provide cross-sectional images with structural-level resolution to depths up to about 1 mm, and to differentiate between normal skin morphology and BCC tumor-related disruption: formation of round hypoechic areas, often surrounded by stronger signal, aura-like, caused by the high scattering of the stromal tissue around the tumor nodules. The correlation of OCT images with histology has demonstrated the capability of OCT to accurately retrieve BCC depth margins. No quantitative thresholding algorithm has been used in this preliminary study to analyze the OCT images. The margins of the BCCs have been visually identified by expert readers of OCT images. The pathology-to-OCT correlation has been done by an independent investigator (a pathologist), who can interpret the histology slides and compare the depth spreading with the values indicated by the OCT reader. However, we will also consider in the future the use of an automated segmentation algorithm that might be used to more objectively assess BCC depth spreading.

The use of polarization sensitive OCT (PSOCT) for determining depth margins of BCCs relative to the DE junction was investigated as well. It is known that in most of the areas of the skin on the human body, the DE junction is not well differentiated by reflectance OCT. Therefore, based on the reflectance OCT image alone, it is difficult to determine the depth cancer margin relative to the DE junction. This is important to know when selecting the therapy strategy. It was concluded that PSOCT can help to identify the DE junction; thus the phase retardance can augment the reflectance image. However, it was also noted that the disruption of the orientation of the collagen fibers by cancer resulted in inconsistent phase retardance within the BCC nodular areas, thus phase retardance image alone cannot be used to accurately measuring BCC spreading depth.

Tumors with depths of over 700 μm were not accurately evaluated by our current OCT instrument because the deeper imaging capabilities were limited by the relatively high NA of the imaging objective ($\sim$0.2 in the OCT mode), which limits OCT imaging depth, as well as by the relatively high roll-off of the sensitivity of the dual channel spectrometer ($>$5 dB/mm) used in our PSOCT instrument. Therefore, as stated above, a compromise has to be made between the desired RCM resolution and OCT imaging depth, such that an adequate NA imaging objective must be selected as a function of the overall thickness of the investigated area of the skin. Furthermore, a better-engineered instrument with improved depth decay of sensitivity may help to overcome or at least lessen this problem.

Beyond this benchtop study, the next step is in progress: to construct a handheld RCM/OCT device with which we will proceed to testing on patients with more rigorous statistical correlation to pathology. We are currently designing a new instrument that will provide better contrast in brightfield reflectance mode (with reduced speckle noise) and increased imaging depth (over 1.2 mm), as well as with improved axial/lateral resolution (6 μm in air). In the long term, with such an imaging-guided approach for treatment of superficial and early nodular BCCs, patients may benefit, per year, from less invasive, lower-cost, newer, and more effective therapeutic alternatives to traditional surgery.

References

1. H.W. Rogers et al., "Incidence estimate of nonmelanoma skin cancer in the United States, 2006," *Arch. Dermatol.* **146**(3), 283–287 (2010).
2. A. Lomas, J. Leonardi-Bee, and F. Bath-Hextall, "A systematic review of worldwide incidence of nonmelanoma skin cancer," *Br. J. Dermatol.* **166**(5), 1069–1080 (2012).
3. A. Wysong et al., "Nonmelanoma skin cancer visits and procedure patterns in a nationally representative sample: national ambulatory medical care survey 1995–2007," *Dermatol. Surg.* **39**(4), 596–602 (2013).
4. S. Deady, L. Sharp, and H. Comber, "Increasing skin cancer incidence in young, affluent, urban populations: a challenge for prevention," *Br. J. Dermatol.* **171**(2), 3214–3231 (2014).
5. S. J. Miller and J. M. Moresi, "Actinic keratosis, basal cell carcinoma and squamous cell carcinoma," in *Dermatology*, J. L. Bolognia, J. L. Jorizzo, and R. P. Rapini, Eds., pp. 1677–1696, Mosby, London (2008).

6. R. A. Schwartz, "Basal cell carcinoma," in *Skin Cancer Recognition and Management*, R. A. Schwartz, Ed., pp. 87–104, Blackwell, Massachusetts (2008).

7. K. Nouri et al., "Basal cell carcinoma," in *Skin Cancer*, K. Nouri, Ed., pp. 61–85, McGraw Hill, New York (2007).

8. M. M. Chren et al., "Recurrence after treatment of nonmelanoma skin cancer: a prospective cohort study," *Arch. Dermatol.* **147**(5), 540–546 (2011).

9. E. P. Tierney and C. W. Hanke, "Cost effectiveness of Mohs micrographic surgery: review of the literature," *J. Drugs Dermatol.* **8**(10), 914–922 (2009).

10. L. Ravitskiy, D. G. Brodland, and J. A. Zitelli, "Cost analysis: Mohs micrographic surgery," *Dermatol. Surg.* **38**(4), 585–594 (2012).

11. L. Brightman et al., "Do lasers or topicals really work for nonmelanoma skin cancers?," *Semin. Cutaneous Med. Surg.* **30**(1), 14–25 (2011).

12. S. Iyer et al., "Full face laser resurfacing: therapy and prophylaxis for actinic keratoses and non-melanoma skin cancer," *Lasers Surg. Med.* **34**(2), 114–119 (2004).

13. R. Smucler and M. Vlk, "Combination of Er:YAG laser and photodynamic therapy in the treatment of nodular basal cell carcinoma," *Lasers Surg. Med.* **40**(2), 153–158 (2008).

14. C.J. Chen et al., "Confocal microscopy guided laser ablation for superficial and early nodular basal cell carcinoma," *JAMA Dermatol.* **150**(9), 994–998 (2014).

15. K. Kose et al., "Video-mosaicing of reflectance confocal images for examination of extended areas of skin in vivo," *Br. J. Dermatol.* **171**(5), 1239–1241 (2014).

16. C. A. Lieber et al., "In vivo nonmelanoma skin cancer diagnosis using Raman microspectroscopy," *Lasers Surg. Med.* **40**(7), 461–467 (2008).

17. N. Neittaanmäki-Perttu et al., "Detecting field cancerization using a hyperspectral imaging system," *Lasers Surg Med.* **45**(7), 410–417 (2013).

18. E. Drakaki et al., "Spectroscopic methods for the photodiagnosis of nonmelanoma skin cancer," *J. Biomed. Opt.* **18**(6), 061221 (2013).

19. C. A. Banzhaf et al., "Optical coherence tomography imaging of non-melanoma skin cancer undergoing imiquimod therapy," *Skin Res. Technol.* **20**, 170–176 (2014).

20. J. Paoli, M. Smedh, and M. B. Ericson, "Multiphoton laser scanning microscopy–a novel diagnostic method for superficial skin cancers," *Semin. Cutaneous Med. Surg.* **28**(3), 190–195 (2009).

21. R. Patalay et al., "Multiphoton multispectral fluorescence lifetime tomography for the evaluation of basal cell carcinomas," *PLoS One* **7**(9), e43460 (2012).

22. M. Manfredini et al., "High-resolution imaging of basal cell carcinoma: a comparison between multiphoton microscopy with fluorescence lifetime imaging and reflectance confocal microscopy," *Skin Res. Technol.* **19**(1), e433–e443 (2013).

23. R. Alkalay et al., "Fluorescence imaging for the demarcation of basal cell carcinoma tumor borders," *J. Drugs Dermatol.* **7**(11), 1033–1037 (2008).

24. E. S. Flores et al., "Intraoperative imaging during Mohs surgery with reflectance confocal microscopy: initial clinical experience," *J. Biomed. Opt.* **20**(6), 061103 (2015).

25. S. A. Alawi et al., "Optical coherence tomography for presurgical margin assessment of non-melanoma skin cancer - a practical approach," *Exp. Dermatol.* **22**(8), 547–551 (2013).

26. F. Bobadilla et al., "Pre-surgical high resolution ultrasound of facial basal cell carcinoma: correlation with histology," *Cancer Imaging* **8**, 163–172 (2008).

27. A. Jambusaria-Pahlajani et al., "Test characteristics of high-resolution ultrasound in the preoperative assessment of margins of basal cell and squamous cell carcinoma in patients undergoing Mohs micrographic surgery," *Dermatol. Surg.* **35**(1), 9–16 (2009).

28. M. Nassiri-Kashani et al., "Pre-operative assessment of basal cell carcinoma dimensions using high frequency ultrasonography and its correlation with histopathology," *Skin Res. Technol.* **19**(1), e132–e138 (2013).

29. Z. Y. Pan et al., "In vivo reflectance confocal microscopy of Basal cell carcinoma: feasibility of preoperative mapping of cancer margins," *Dermatol. Surg.* **38**(12), 1945–1950 (2012).

30. K. X. Wang et al., "Optical coherence tomography-based optimization of Mohs micrographic surgery of basal cell carcinoma: a pilot study," *Dermatol. Surg.* **39**(4), 627–633 (2013).

31. S.-Y. Jeon, K.-H. Kim, and K.-H. Song, "Efficacy of photodynamic diagnosis-guided Mohs micrographic surgery in primary squamous cell carcinoma," *Dermatol. Surg.* **39**(12), 1774–1783 (2013).

32. E. Tierney, J. Petersen, and C. W. Hanke, "Photodynamic diagnosis of tumor margins using methyl aminolevulinate before Mohs micrographic surgery," *J. Am. Acad. Dermatol.* **64**(5), 911–918 (2011).

33. M. Carducci et al., "Margin detection using digital dermatoscopy improves the performance of traditional surgical excision of basal cell carcinomas of the head and neck," *Dermatol. Surg.* **37**(2), 280–285 (2011).

34. S. G. Gonzalez, M. Gill, and A.C. Halpern, *Reflectance Confocal Microscopy of Cutaneous Tumors–An Atlas with Clinical, Dermoscopic and Histological Correlations*, pp. 1–6, Informa Healthcare, London (2008).

35. P. Guitera et al., "In vivo reflectance confocal microscopy enhances secondary evaluation of melanocytic lesions," *J. Invest. Dermatol.* **129**, 131–138 (2009).

36. Z. Tannous, A. Torres, and S. Gonzalez, "In vivo real-time confocal reflectance microscopy: a noninvasive guide for Mohs micrographic surgery facilitated by aluminum chloride, an excellent contrast enhancer," *Dermatol. Surg.* **29**(8), 839–846 (2003).

37. S. A. Webber et al., "Effectiveness and limitations of reflectance confocal microscopy in detecting persistence of basal cell carcinomas: a preliminary study," *Australas. J. Dermatol.* **52**(3), 179–185 (2011).

38. S. Nori et al., "Sensitivity and specificity of reflectance mode confocal microscopy for in vivo diagnosis of basal cell carcinoma: a multicenter study," *J. Am. Acad. Dermatol.* **51**, 923–930 (2004).

39. Z. Y. Pan et al., "In vivo reflectance confocal microscopy of basal cell carcinoma: feasibility of preoperative mapping of cancer margins," *Dermatol. Surg.* **38**(12), 1945–1950 (2012).

40. A.-M. Forsea et al., "Clinical application of optical coherence tomography for the imaging of non-melanocytic cutaneous tumors: a pilot multi-modal study," *J. Med. Life* **3**(4), 381–389 (2010).

41. M. Mogensen et al., "Assessment of optical coherence tomography imaging in the diagnosis of non-melanoma skin cancer and benign lesions versus normal skin: observer-blinded evaluation by dermatologists and pathologists," *Dermatol. Surg.* **35**, 965–972 (2009).

42. J. M. Olmedo et al., "Optical coherence tomography for the characterization of basal cell carcinoma in vivo: a pilot study," *J. Am. Acad. Dermatol.* **55**(3), 408–412 (2006).

43. M. R. Avanaki et al., "Investigation of basal cell carcinoma using dynamic focus optical coherence tomography," *Appl. Opt.* **52**(10), 2116–2124 (2013).

44. T. Hinz et al., "Preoperative characterization of basal cell carcinoma comparing tumour thickness measurement by optical coherence tomography, 20-MHz ultrasound and histopathology," *Acta Derm. Venereol.* **92**(2), 132–137 (2012).

45. C. K. Hitzenberger et al., "Measurement and imaging of birefringence and optic axis orientation by phase resolved polarization sensitive optical coherence tomography," *Opt. Express* **9**(13), 780–790 (2001).

46. T. E. Ustun et al., "Real-time processing for Fourier domain optical coherence tomography using a field programmable gate array," *Rev. Sci. Instrum.* **79**(11), 114301 (2008).

47. C. Blasdale et al., "Effect of tissue shrinkage on histological tumour-free margin after excision of basal cell carcinoma," *Br. J. Dermatol.* **162**(3), 607–610 (2010).

Nicusor Iftimia is a principal research scientist at Physical Sciences Inc., Andover, Massachusetts. He received his BS, MS, and PhD degrees in physical engineering from Bucharest University and his postdoctoral training in biomedical imaging from Clemson University and Harvard Medical School. His current research interests include OCT, confocal microscopy, near-infrared fluorescence imaging, and multimodal imaging, all applied to disease diagnosis and therapy guidance/response monitoring. He is a senior member of SPIE and a senior member of OSA. He is author/coauthor of more than 70 peer-reviewed publications and several book chapters, and is the editor of a book.

Biographies for the other authors are not available.